VISIBLE TO NEAR-INFRARED ANALYSIS OF GRANITES – A METHOD FOR CHARGE COUPLED DEVICE SPECTROSCOPY

Robert S. McEwan

Submitted in partial fulfillment of the requirements
for the degree of Bachelor of Science, Honours
Department of Earth Science
Dalhousie University, Halifax, Nova Scotia
March 2016

Distribution License

DalSpace requires agreement to this non-exclusive distribution license before your item can appear on DalSpace.

NON-EXCLUSIVE DISTRIBUTION LICENSE

You (the author(s) or copyright owner) grant to Dalhousie University the non-exclusive right to reproduce and distribute your submission worldwide in any medium.

You agree that Dalhousie University may, without changing the content, reformat the submission for the purpose of preservation.

You also agree that Dalhousie University may keep more than one copy of this submission for purposes of security, back-up and preservation.

You agree that the submission is your original work, and that you have the right to grant the rights contained in this license. You also agree that your submission does not, to the best of your knowledge, infringe upon anyone's copyright.

If the submission contains material for which you do not hold copyright, you agree that you have obtained the unrestricted permission of the copyright owner to grant Dalhousie University the rights required by this license, and that such third-party owned material is clearly identified and acknowledged within the text or content of the submission.

If the submission is based upon work that has been sponsored or supported by an agency or organization other than Dalhousie University, you assert that you have fulfilled any right of review or other obligations required by such contract or agreement.

Dalhousie University will clearly identify your name(s) as the author(s) or owner(s) of the submission, and will not make any alteration to the content of the files that you have submitted.

If you have questions regarding this license please contact the repository manager at dalspace@dal.ca.

Grant the distribution license by signing and dating below.

_____ _____

Name of signatory Date

Distribution License

DalSpace requires agreement to this non-exclusive distribution license before your item can appear on DalSpace.

NON-EXCLUSIVE DISTRIBUTION LICENSE

You (the author(s) or copyright owner) grant to Dalhousie University the non-exclusive right to reproduce and distribute your submission worldwide in any medium.

You agree that Dalhousie University may, without changing the content, reformat the submission for the purpose of preservation.

You also agree that Dalhousie University may keep more than one copy of this submission for purposes of security, back-up and preservation.

You agree that the submission is your original work, and that you have the right to grant the rights contained in this license. You also agree that your submission does not, to the best of your knowledge, infringe upon anyone's copyright.

If the submission contains material for which you do not hold copyright, you agree that you have obtained the unrestricted permission of the copyright owner to grant Dalhousie University the rights required by this license, and that such third-party owned material is clearly identified and acknowledged within the text or content of the submission.

If the submission is based upon work that has been sponsored or supported by an agency or organization other than Dalhousie University, you assert that you have fulfilled any right of review or other obligations required by such contract or agreement.

Dalhousie University will clearly identify your name(s) as the author(s) or owner(s) of the submission, and will not make any alteration to the content of the files that you have submitted.

If you have questions regarding this license please contact the repository manager at dalspace@dal.ca.

Grant the distribution license by signing and dating below.

_____ _____

Name of signatory Date

Abstract

Visible to near-infrared analysis of granites – a method for charge coupled device spectroscopy

Robert S. McEwan
Department of Earth Science, Dalhousie University, Halifax, N.S., B3H 4R2
rb383752@dal.ca

An area of leucomonzogranite, north of Herring Cove, Nova Scotia provides a well exposed section of nearly continuous outcrop used as a test of a remotely sensed image analysis. The objective is to examine the effectiveness of a charge coupled device (CCD) in producing whole rock spectra based on average pixel values, and in the identification of absorption features in hand samples. Three test sites were imaged using a near-infrared (NIR) converted Nikon D40 SLR camera with filters in the blue, green, red, and NIR range. Samples from each test site were imaged at a fine (mm) scale using a bellows, with the same filters as the field test sites. A NIR removal method was determined to correct color filtered images with additional transmission in the NIR region. Image analysis revealed that spectral variation in the NIR region is controlled by biotite and quartz content, which occur as millimeter sized clusters in outcrop samples. An NDVI calculation was used to separate lichen and surface depression pixels from outcrop pixels to compile a spectra for each outcrop site.

Error in the results are reported as wavelength specific over-compensation and under-compensation from the NIR removal process, and non-linear detection of NIR light on the sensor versus exposure time. Overexposure and camera drift are field specific sources of error.

Keywords: Halifax pluton; remote sensing; charge coupled device; image processing; multispectral analysis; absorption bands; imaging spectroscopy

Contents

Table of Tables

Table of Figures

Acknowledgements

I would like to extend my gratitude to the entire Dalhousie Earth Sciences Department for providing me with the support and the inspiration to bring this project together. Particularly, I would like to thank Thomas Duffett for his assistance in cutting samples and finding a space for me to collect my data. To my friends and family, whose help and support is the reason I am where I am today. Finally to Charles Walls, without his expertise, unwavering support and commitment, the wealth of learning and inspiration that stemmed from this experience would not have been possible.

1.0 INTRODUCTION

Multispectral imaging is a valuable tool in the geosciences. Airborne and satellite platforms use remotely sensed, multispectral images to detect and map alteration minerals associated with ore deposits. Reflective and absorptive habits of individual minerals are measured using a spectrometer, generally using either Fourier transform infrared spectroscopy (FTIR) or Raman spectroscopy.

When electromagnetic (EM) energy is directed onto a mineral, some is absorbed, some passes through, and some is reflected. Every mineral has a specific absorbance spectrum with a shape that is dependent upon the distances and angles between atoms, their relative atomic masses, and atomic radii. These factors are determined by the arrangement of anions and cations in the crystal lattice, which form a regular, repeating pattern in the mineral structure, vibrating at specific frequencies. Absorption of energy is possible when positive and negative ions move out of phase with each other. The ionic movement creates a vibrational frequency matching the wavelength of energy that can be absorbed, as long as a net dipole moment occurs (Hamilton, V.E., 2010).

Spectra can be scaled up to whole rock analysis. The similarities between reflectance and absorbance spectra of different crystalline rock types are characterized by an inverse relationship when plotted against EM wavelengths (Lyon, R.J.P., et al. 1963). One of the issues facing whole rock analysis using reflectance or absorbance spectra is that variations in grain size will affect the amplitude of spectral readings (Feng, J., et al. 2011). Generally, the aim is to use laboratory measurements to calibrate

remotely sensed airborne and satellite images to cost effectively collect geological outcrop data, including rock type classification, alteration, and mineralogical changes.

The purpose of this study is to obtain multispectral images of small, crystalline rock samples, generate an average pixel value indicative of the whole rock composition, and build a spectral signature from average pixel values obtained at different wavelengths of reflected light. We investigate the ability to replicate this signature at different scales, from the fine (mm) scale to coarse (1-2 m) scale with the intent to detect compositional variation among outcrops in the Halifax Pluton.

2.0 BACKGROUND

2.1 The Remote Sensing Process

The passive remote sensing process (figure 2-1) records reflected light from an EM emitting source. Reflectance can be perfectly specular (all incident light is reflected at the angle it hits a surface) like a mirror, perfectly diffuse (light scatters in all directions once it reaches a surface), or more commonly in between the two. The sun generates shortwave EM energy via thermonuclear fusion with a peak intensity that occurs in the visible light region (Jensen, 2005). When light enters the Earth's atmosphere, some travels directly to the surface (1 to 3), and some scatters and absorbs due to interaction with particles in the atmosphere. At location 3 in figure 2-1, light incident on the surface can also originate from photons that have already interacted with atmospheric particles (possibly changing their polarization and spectral characteristics) or from light that already reflected off of a different surface, scattered in the atmosphere, and reflected again off of the surface (Jensen, 2005). Further scattering and absorption occurs between the sensor and reflector (4). All

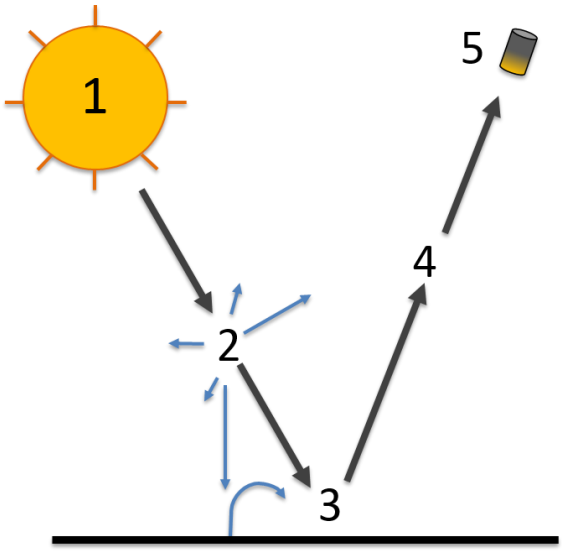

Figure 2-1. The passive remote sensing process. 1) An EM radiation emitting source. 2) Interaction with atmospheric particles and scattering of light. 3) Reflection surface. 4) Reflected light path and further scattering. 5) Sensor

parts of the path affect the spectral composition of the signal, which is detected at the sensor, registering the amount of radiance at different wavelengths (5).

2.2 Digital Photography

The charge coupled device (CCD) is the sensor responsible for generating digital images (figure 2-2). The CCD has an array of photosites that correspond to the pixels in an image. Photosites are metal-oxide semiconductor (MOS) diodes regulated by clock voltage pulses that trap electrons and transfer them down the chain of diodes (Fujiwara and Takahasi, 2001). The MOS diodes are placed over a thin layer of silicon dioxide grown on top of a silicon wafer (Healey and Kondepudy, 1994). When the camera shutter opens, light hits the sensor and the photon-silicon interactions at each photosite generate an electron hole pair (Healey and Kondepudy, 1994). Applying a positive electrical potential to the array of MOS diodes enables electrons to be stored as groups (Healey and Kondepudy, 1994). During transfer, the charge groups maintain separation, however only a fraction of the charge is able to transfer from photosite to photosite. The effectiveness of this process at preserving the original charge is called the charge transfer efficiency (CTE) of a particular device (Healey and Kondepudy, 1994). Once the charge groups are collected, the information is converted to a signal in the CCD output register (Jenson,

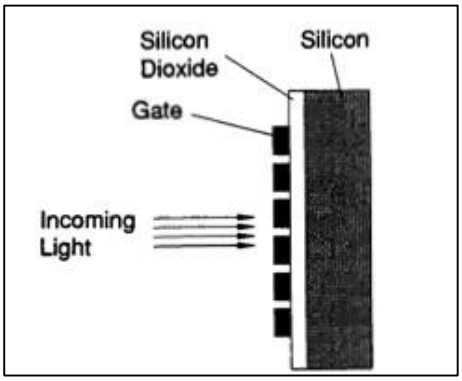

Figure 2-2. Diagram of a CCD sensor from Holst (1998). Gates are referred to as MOS diodes in text.

J.R. 2005). The signal is then digitized and stored in either the camera's internal memory or on an SD card, to be displayed as pixels in raster format (Jenson, J.R. 2005). Raster images are built from a pixel array based on the charge groups obtained from the CCD sensor. Some cameras use a complementary metal-oxide-semiconductor (CMOS) sensor to build raster images. CMOS utilizes a similar 2D pixel array to CCDs, however charge is converted to voltage directly at the photosite (Litwiller, 2005).

Sensors vary from manufacturer to manufacturer both in the configuration of the array and in the spectral response (Holst, 1998). Specialized systems use a three-CCD configuration where incoming light is spectrally separated through filters and coated beam splitters (Holst, 1998). Most consumer cameras use single CCD systems with a configuration of filters that cover the MOS diodes (figure 2-3). The stripe system aligns filters into a repeating system of columns or rows, whereas the mosaic system involves an arrangement of filtered diodes in a type of color filter matrix. In both cases, the ratio of red to green to blue diodes may not be equal, and it

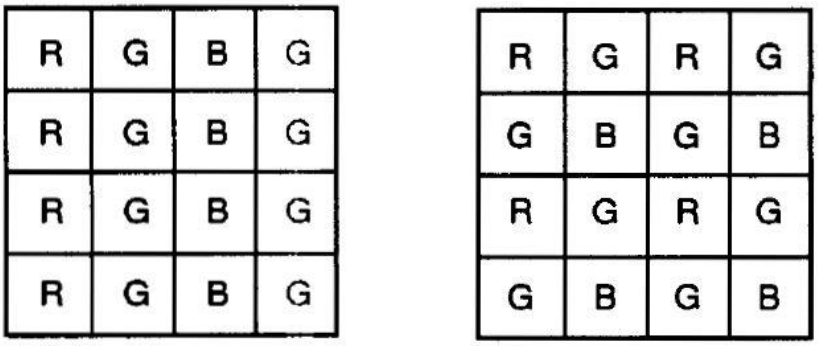

Figure 2-3. Single CCD sensor array configuration. The two types of systems are a) the stripe system that arranges filters into columns or rows and b) the mosaic system that has a repeating matrix of filtered pixels.

is common for sensors to have twice as many green diodes as red and blue diodes (Holst, 1998).

After the detection process, each pixel has a single value based on the intensity of light that is reflected off of a surface. The intensity value corresponds to how dark or bright a certain color will appear in the pixel. In monochromatic light for example, a completely black image has all pixel values of 0. A completely white image has all pixel values of 255. All other values from 1-254 indicate values of grey that gradually decrease in darkness.

CCD sensors are also sensitive to ultraviolet (UV) and infrared (IR) wavelengths of light, in addition to the visible (~430 to 680 nm) wavelengths of the electromagnetic (EM) spectrum (Holst, 1998). Camera sensors are fitted with IR blocking filters so that the CCD only detects wavelengths in the visible spectrum (Lifepixel, 2015). Glass transmittance is nearly 0% below the 300 nm level. Above 400 nm and well into the near infrared (NIR) range, glass transmits close to 90% of incoming EM energy (Naganuma, Kagawa, 1999).

2.3 CCD Noise

Ideally, the CCD sensor only registers incident photons from the reflecting surface and converts this data into pixels. This however is not the case, and there are a variety of noise sources related to this type of sensor.

Dark current is caused by the interaction of thermal energy with the silicon sensor (Healey and Kondepudy, 1994; Holst, 1998), which causes free electrons to

be generated and registered at photosites as if they were photon-generated electrons (Healey and Kondepudy, 1994). Healey and Kondepudy (1994) state that the level of noise associated with dark current is proportional to the integration time. Holst (1998) states that there are three sources of thermally generated dark current – generation in the depletion region, generation and diffusion in the bulk material, and generation due to surface states. Both authors agree that dark current can be greatly reduced by cooling the sensor, to the point that dark current generation can be reduced to "less than one electron per collection site per second" (Healey and Kondepudy, 1994).

Blooming is a source of noise caused by overexposing photosites (Healey and Kondepudy, 1994). Sensors generally have overflow drains either attached to each pixel or attached to a column of pixels (Holst, 1998). The purpose of these drains is to prevent charge overflow from corrupting surrounding photosites. However if charge overflow is too severe to be contained by the overflow drains, surrounding pixels yield skewed values.

Shot noise is the uncertainty related to the amount of photons that arrive and are detected by CCD photosites (Galbán et al., 2010; Healey and Kondepudy, 1994; Holst, 1998). Galbán et al. (2010) state that the amount of shot noise is independent of the sensor temperature. Healey and Kondepudy (1994) report that shot noise forms a Poisson distribution and is impossible to eliminate, although both Healey and Kondepudy (1994) and Holst (1998) report that the amount of shot noise is related to the amount of dark current present.

2.4 Lichen Coverage

Lichen commonly occurs in the study region encrusting variable portions of SMB outcrops. This is problematic for a reflected light analysis of outcrops because lichen species transmit little to no light in the visible to NIR regions (Ager and Milton, 1987, citing Gates, 1980; Bechtel et al., 2002). Ager and Milton (1987) studied the spectral reflectance of lichens and rock substrates and referenced two conclusions of Hale (1983): 1) the lithology of the rock substrate largely dictates the composition of the lichen community inhabiting it, and 2) substrate factors result in 60 percent of lichen variation while 40 percent is dictated by microclimate. Lichen reflectance does not show any significant peaks in the 400 nm to ~1400 nm range, with the exception of a shallow feature around the 660 nm to 680 region attributed to chlorophyll absorption (Ager and Milton, 1987; Bechtel et al, 2002; Rees et al 2003). Ager and Milton (1987) report a strong water absorption band at 1400 nm. Rees et al (2003) and Bechtel et al (2002) both report strong water absorption bands at 1450 – 1465 nm range and 1445 nm respectively. Variation in the absorption bands is likely the result of variation in lichen species and/or analytical techniques.

Vegetation (chlorophyll) strongly absorbs red light and reflects NIR light (Nemani and Running, 1989). The Normalized Difference Vegetation Index (NDVI) integrates this feature to separate vegetation from other surface types by the following calculation: NDVI = [(NIR-Red)/(NIR+Red)], where water, clouds, and

snow have negative values, rock and soil generate values near zero, and increasing chlorophyll content approaches a value of 1 (Olthof et al., 2008).

2.5 Absorption Bands

Mineral absorption bands are caused by bond vibrations, ionic charge transfer, electronic transitions, and conduction processes (Clarke et al, 1990). In the visible to NIR region, absorption bands take the form of broad features related to ligand field transitions and metal-metal charge transfers (Clarke et al. 1990). Lyon and Burns (1963) acquired reflectance spectra from a variety of igneous rock types in the IR spectrum and determined that major peak shifts are attributed to bulk composition variations between rock types, and smaller peaks correspond to specific minerals present in the samples. Smith (1978) references Faye (1968) and Robbins and Strens (1972), stating that the basal section of biotite displays three absorption bands in the NIR region (1111 nm, 909 nm, and 714 nm). Smith (1978) also reports that these bands are the result of Fe^{2+} - Fe^{3+} interactions and can be largely increased in intensity if the sample temperature is reduced (from 550°C to

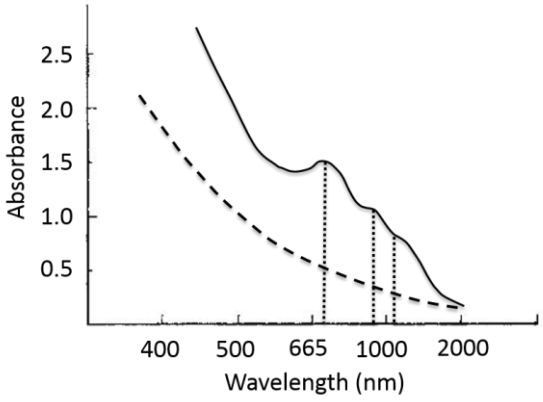

Figure 2-4. Basal biotite spectra adapted from Smith (1978). Solid line indicates room temperature spectrum and dashed line is the sample heat treated at 550°C for 6 hours. Dotted vertical lines indicate previously reported iron absorption bands.

room temperature in the Smith (1978) study) (figure 2-4).

In plagioclase, Fe^{3+} produces a distinct absorption band at 860 nm and a steep absorption feature at 600 nm, however Fe^{3+} concentrations in plagioclase are not commonly high enough to display these bands (Adams and Goullaud, 1978). Adams and Goullaud (1978) reference Longhi et al. (1976), reporting that occurrence of Fe^{2+} in plagioclase is mainly caused by substitutions in the Al sites (or less commonly in the Ca sites). Adams and Goullaud. (1978) further states, in reference to Adams (1975) that Fe^{2+} is sensitive to crystal field effects, and the change in absorption band intensities at its centered wavelength may enable the determination of plagioclase composition due to crystal structure changes in the solid solution series (figure 2-5).

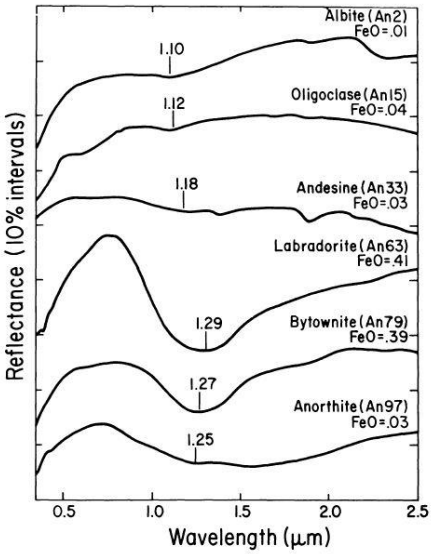

Figure 2-5. . Wavelength centers of iron absorption bands in plagioclase from Adams and Goullaud (1978). Reflectance intensity in the visible region is a function of both iron content and endmember composition.

Rare earth element (REE) oxides have distinct features in the visible to NIR region (figure 2-6) (Clarke et al., 1993; Clarke, 1999; Kerr et al., 2011). Clarke (1999) also states that REE absorption bands are the result of unfilled electron shells, which alters the spectral signature of the mineral they are present in.

The strong Si – O absorption bands in quartz appear in the 8000 to 10 000 nm range (Lyons, 1965; Ninomiya et al, 2005) and are outside of the spectral range in this study.

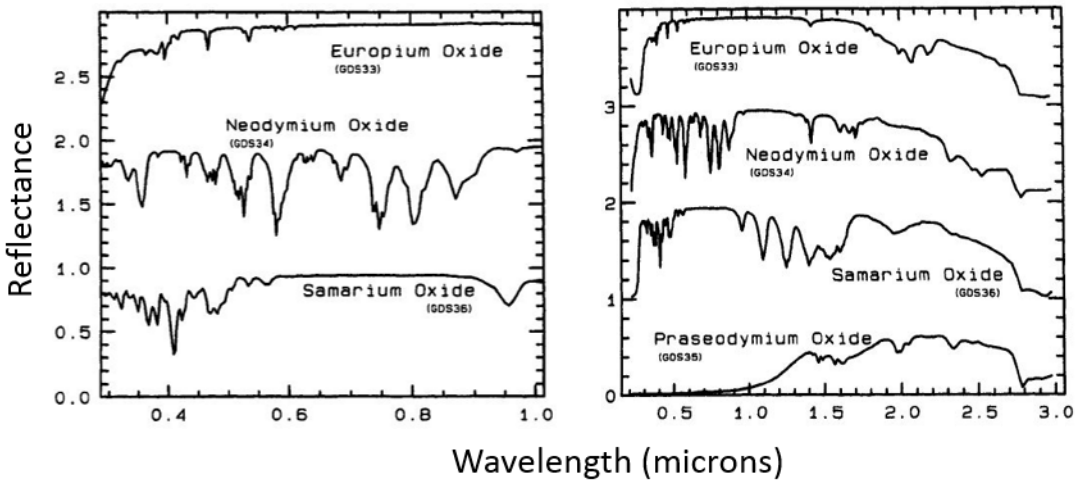

Figure 2-6. Rare earth element oxide spectra in the visible to NIR region. From Clarke et al., (1993).

2.6 Nova Scotia Granites

The South Mountain Batholith (SMB) extends from Halifax to just east of Yarmouth, covering an area of ~7300 km^2 (Macdonald, 2001). The batholith is mainly granodiorite and monzogranite in composition, post tectonic, and peraluminous (Clarke and Clarke, 1998). The peraluminous nature of the batholith is attributed to partial melting of the surrounding country rocks, and fractional crystallization is identified as the most significant petrogenetic mechanism (Macdonald and Horne, 1988). The SMB is also the largest granitic body in the Appalachian Orogen (Macdonald, 2001). Smith and Turek (1976) and Macdonald and Horne (1988) argue that the SMB evolved as a multi-sequence batholith with discrete plutons intruding separately from the more primitive SMB sequence. Mackenzie and Clarke (1975) suggest that the SMB was emplaced as one single body

and mineralogical variations are the result of fractionation after emplacement. Macdonald (2001) divides the batholith into Stage I (early) and Stage II (late) plutons, aligning with the multi-sequence emplacement theory. The early and late stage plutons both indicate a calk-alkaline magma source based on chemical, textural, and mineralogical data (Cormier and Smith, 1973; Smith, 1974). This paper focuses on variations in the Halifax Pluton (HP). MacDonald and Horne (1988) conclude that the HP developed as a separate body in the SMB, with an early and late-stage intrusive suite. MacDonald and Horne (1988) also state that the HP, along with the SMB have a partially melted crustal source and suggest a sedimentary origin. Miller (1979) concludes that the HP is composed of pelitic metasedimentary source material.

3.0 METHODS

3.1 General Statement

The aim of this study is to investigate a minimalist approach to full image spectroscopy with an IR converted consumer digital camera and filters to analyze reflected features of the red, green, blue, and near infrared (NIR) wavelengths of light. The method incorporates spectra obtained from fine scale bellows images and coarse scale outcrop images and analyzes the feasibility of maintaining a spectral signature between the two scales. Spectra are based off of average pixel values from filtered images, with the average values plotted as a function of increasing wavelength. Where disparities exist, images can be analyzed visually to determine the effects of mineralogical variation and orientation, surface roughness, and alteration products.

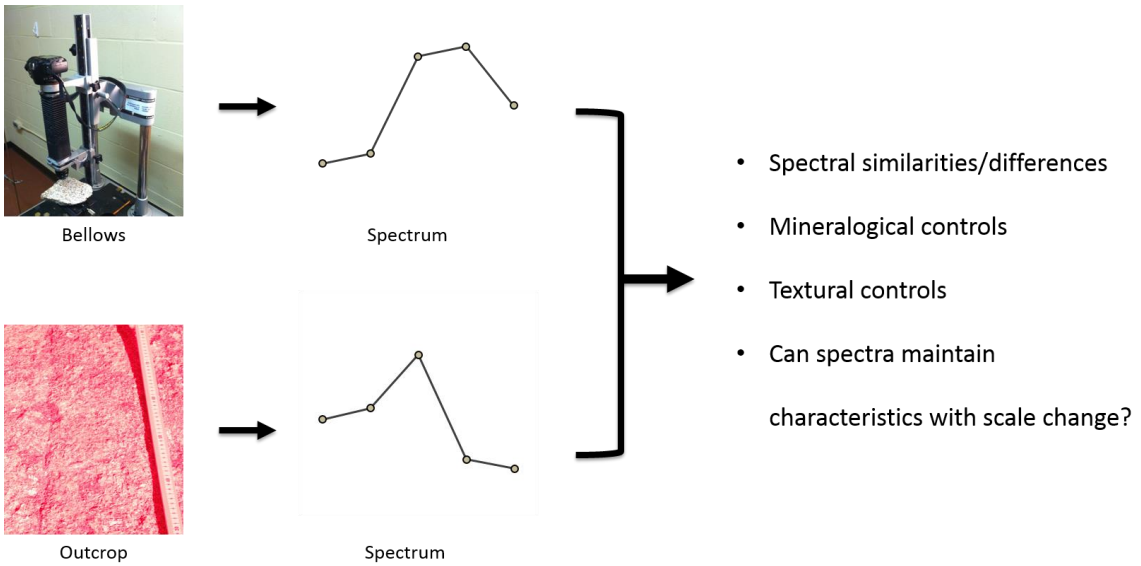

Figure 3-1. A general process overview of the study.

3.2 Camera Conversion

A Nikon D40 SLR was disassembled inside a plastic container to reduce the possibility of dust buildup on the electronics. Ribbon connectors were disconnected and wires were desoldered to enable access to the CCD sensor. It was determined at this point that the system uses a single sensor CCD array. The sensor had a metal brace attached to keep the stock infrared filter in place. Once the brace was

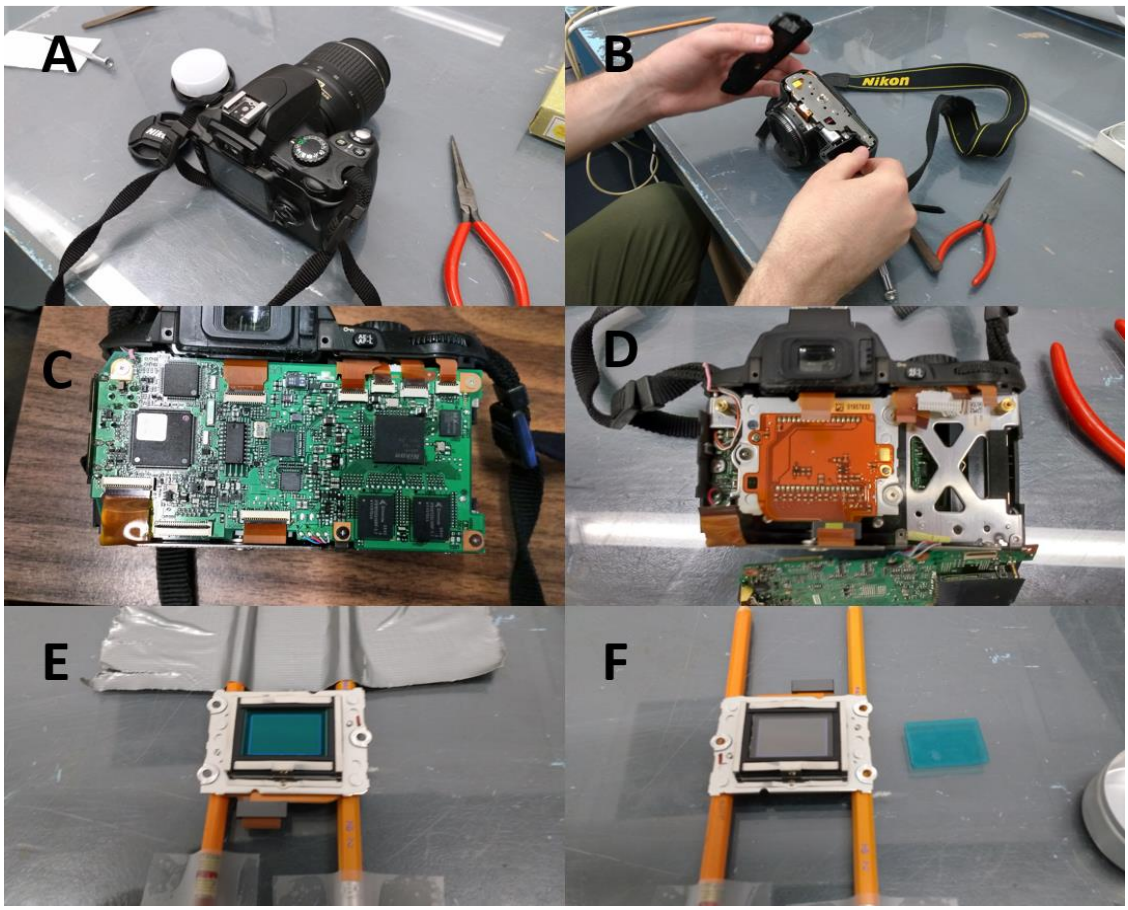

Figure 3-1. Camera conversion process. A) The Nikon D40 SLR before conversion. B) Removal of the lower plate. C) Camera circuit board with ribbon connectors. D) Back section of the CCD sensor. E) CCD with metal brace and IR filter. F) CCD with IR filter replaced by glass cover slip.

removed, the IR filter was also removed, and replaced with a glass cover slip to protect the exposed CCD from future dust contamination. The dimensions of the IR filter were measured. A fresh glass cover slip was cut to size. The cut cover slip was placed over the CCD and secured using the metal brace. The camera was reassembled and tested.

Five polyester filters are used in this study: Tri-Blue (#47B), Tri-Green (#58), Tri-Red (#25), and two IR filters, #87 and #87C, all manufactured by LEE Filters.

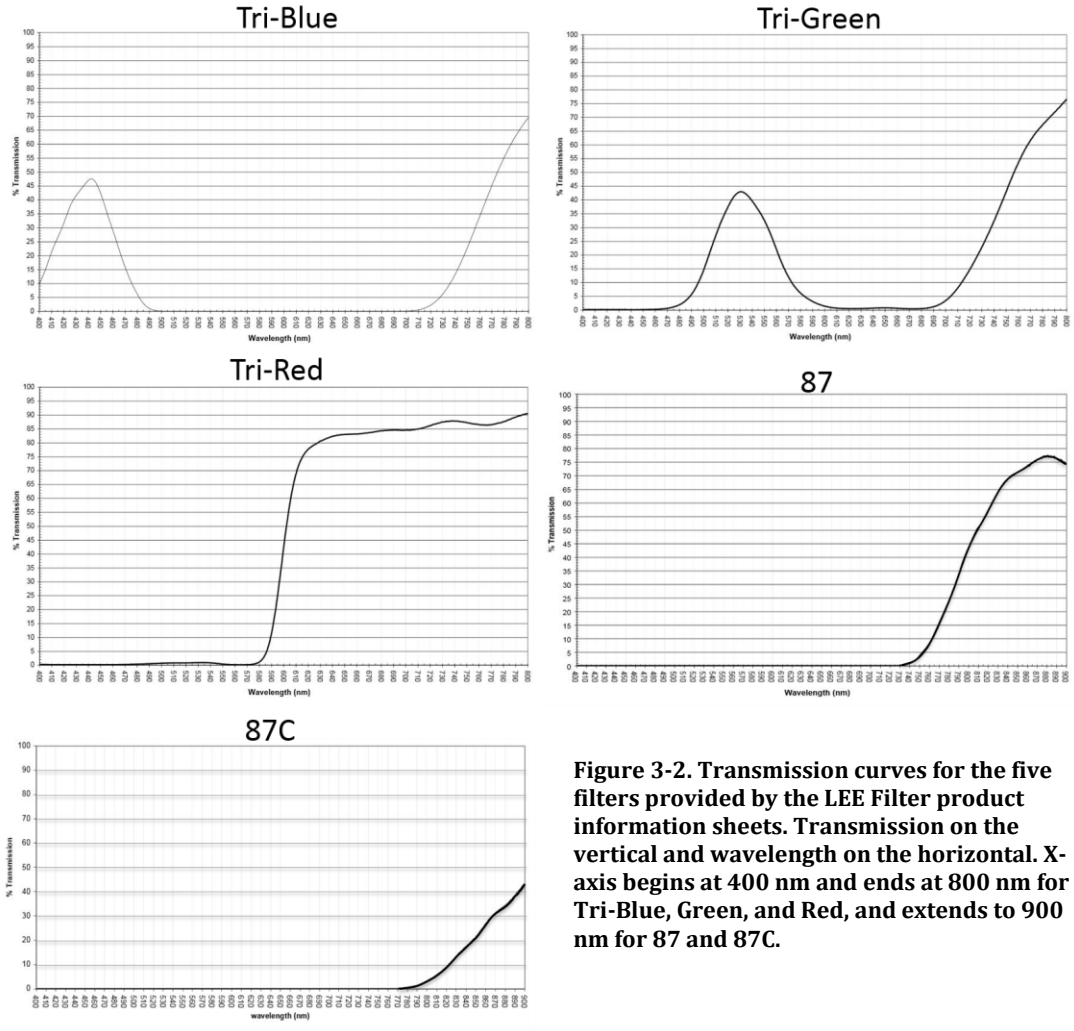

Figure 3-2. Transmission curves for the five filters provided by the LEE Filter product information sheets. Transmission on the vertical and wavelength on the horizontal. X-axis begins at 400 nm and ends at 800 nm for Tri-Blue, Green, and Red, and extends to 900 nm for 87 and 87C.

Curves provided by LEE Filter product information sheets detail the amount of light transmission expected from each filter. The curves only show transmissions up to a wavelength of 900 nm (figure 3-3), and further measurements are required.

3.2 Sensitivity Measurements

The D40 CCD's spectral sensitivity had to be determined as a reference for the field images. An Acrylonitrile Butadiene Styrene (ABS) pipe was cut to 90 cm length and the interior of the pipe was fitted with a rolled up section of black construction paper to reduce internal reflections in the pipe. One end of the pipe was covered except for a thin slit to allow light into the pipe. The other end of the pipe was fitted with a 30° ABS elbow. A circular piece of diffraction grating (500 lines per mm) was cut and placed in the opening of the ABS elbow. A 200W tungsten incandescent bulb was used as the light source, and directed toward the covered end of the pipe with the thin slit. At the other end of the pipe, the Nikon D40 was focused on the diffraction grating to obtain an image of the spectrum from the light source. The spectrum was imaged in the RAW format, first without a filter, then with the 87C filter, 87 filter, tri-red, tri-green, and tri-blue filters (figure 3-4). The camera was not refocused for different filters, however the camera did have to be slightly rotated for the 87 and 87C images.

Exporting from RAW to TIFF separates an image into 3 images, each representing the red, green, and blue portion of the pixel data. This was verified by importing the TIFF images into IDRISI's raster (.rst) format, which allows the separate bands to be viewed individually. IDRISI is a GIS analysis and image processing program incorporated within the TerrSet Geospacial Monitoring and Modelling software system.

Each filtered spectra recorded various amounts of IR across all three bands. Since this was the case for the reference spectra, it was assumed to be the case for field images. The IR response for each group of bands in an image was visually determined.

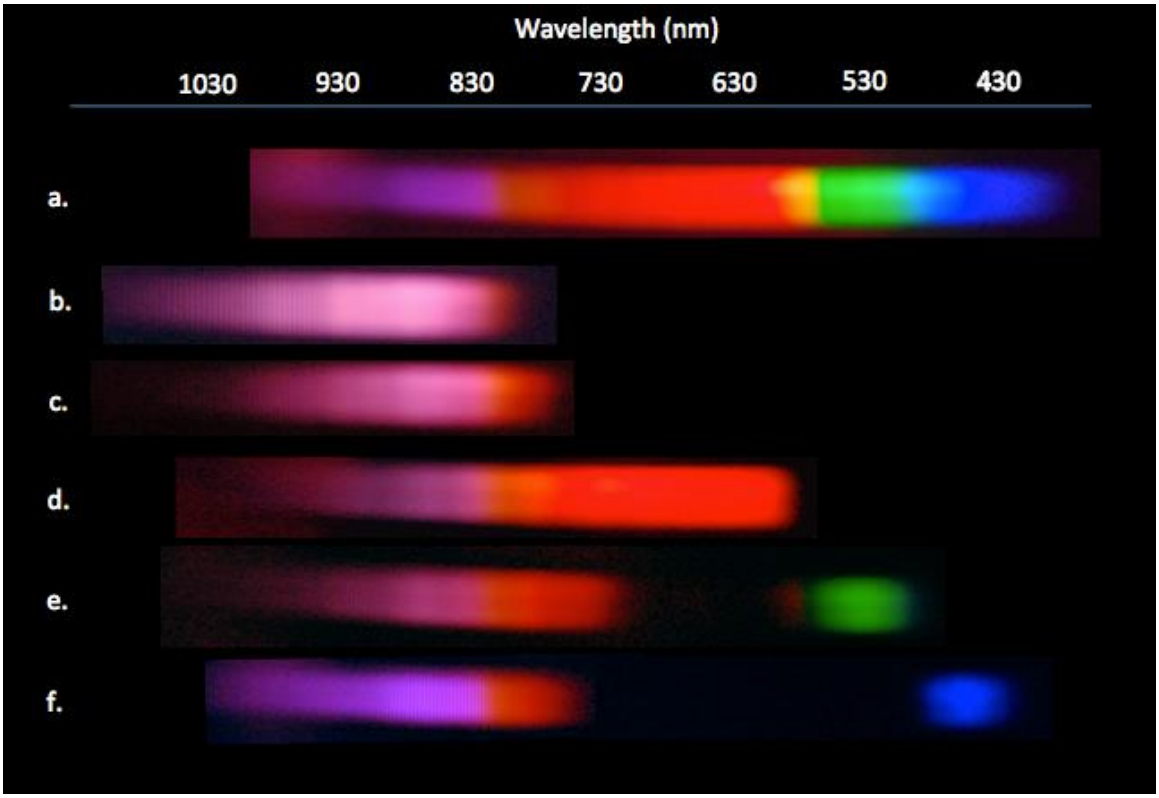

Figure 3-3. Spectral camera sensitivity measurements from an incandescent source. A) Full spectrum, no filters. B) Spectra with the 87C filter. C) 87 filter spectrum. D) Red filter spectrum. E) Green filter spectrum. F) Blue filter spectrum.

3.3 NIR Response Correction

Band 3 of the blue filtered image shows a bimodal peak-response at 440 nm and at ~800 nm. Transmission in the NIR range begins at ~775 nm. By inspection, band 3 of the 87 filter image displayed the most similar NIR transmission range to the blue filtered image. Correcting for exposure differences between the two images, the blue image was multiplied by 0.48125.

It was determined that the average pixel value in the NIR range for each filtered image should be less than 1 compared to the unchanged color values that showed peak transmission values ranging from 230 - 255. This was done for the blue filter image by digitizing a polygon around the region of NIR response. The spatial parameters of the full image were copied to a new image using the INITIAL tool, resetting all pixel values to zero. The RASTERVECTOR tool was then used to combine the NIR polygon (value of 1) with the zeroed image. The 87_3 image was multiplied by a constant and then

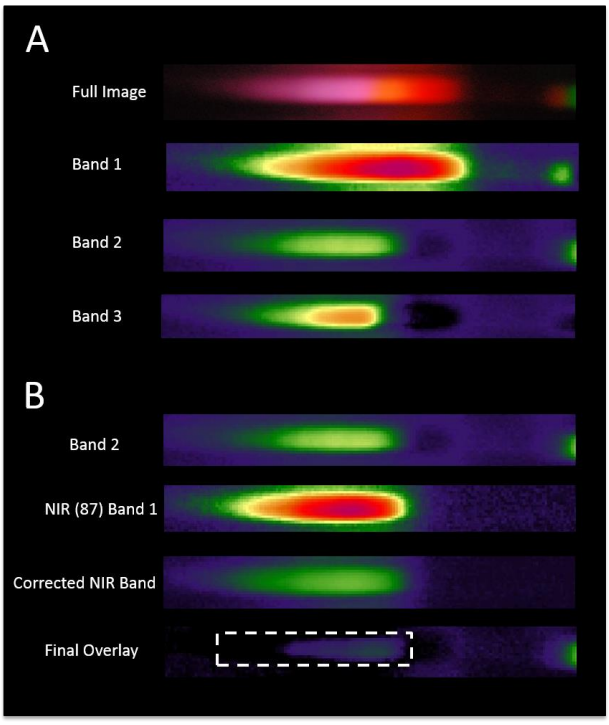

Figure 3-4. Determination of NIR correction constant for green images. A) Full color spectrum (top) in TIFF format and the three separated bands below. B) NIR correction process. The dashed white box indicates the location of NIR polygon image for accuracy measurement.

subtracted from the blue filtered image, using OVERLAY. The OVERLAY process uses a pixel by pixel subtractive algorithm, where a pixel at location (x,y) is subtracted by the pixel contained in the other image at that location. The accuracy was determined by extracting pixel data from the subtracted image under the spatial parameters of the NIR polygon image. This operation created summary statistics of the outlying area and the relevant NIR region. This process was repeated until a constant was found to render an average pixel value in the NIR polygon of less than 1 (table 3-1), corresponding to an average of less than 1 percent NIR transmission compared to the peak blue transmission. NIR removal constants were determined for the green filtered image (figure 3-5) and the red filtered image using the same process, but different constants were required for each filter (table 3-1).

Table 3-1. Shutter correction and NIR removal constants. Band 1 of the 87 filtered image was used for green and red corrections, band 3 was used for the blue correction.

Filter	Shutter Speed (s)	Shutter Correction Factor	NIR Removal Factor	Avg Corrected NIR Pixel Value
87	0.77	null		
Blue	1.6	0.48125	0.81	0.69
87	1/2	null		
Green	1/2	null	0.431	0.43
Red	1/2	null	1.24	0.57

3.4 Outcrop Images

Using the converted SLR camera, a tripod was set up at each sample location to ensure that images for each filer type included the same section of outcrop. A brunton compass was used to determine the angle of the outcrop surface relative to the ground, the angle of the camera relative to the outcrop, and the angle of the sun at each location. Each image was also imaged with a meter stick for scale. A hand sample was collected at each site for macro images to be taken at a larger scale in the lab. Three locations were imaged, two in Spryfield, ~50 m apart, and one in Herring Cove (figure 3-6).

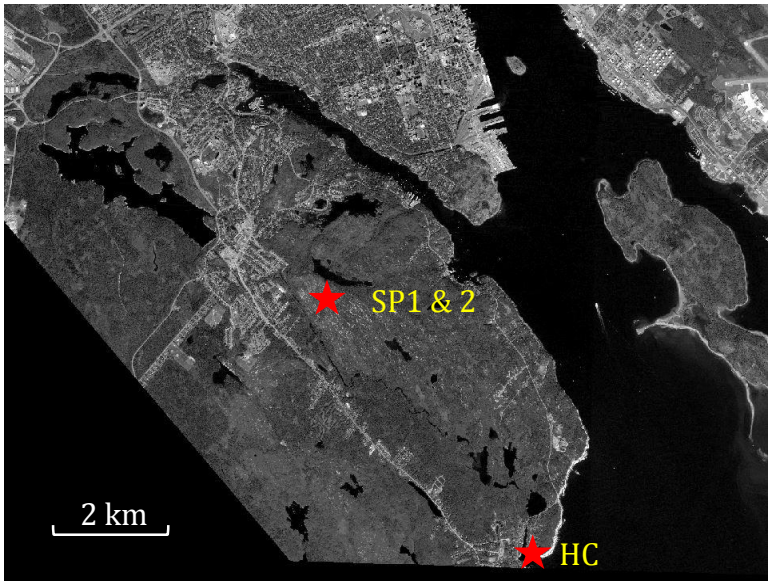

Figure 3-5. Satellite image of study area and locations of Spryfield (SP) outcrops and Herring Cove (HC) outcrops.

Filtered spectral images were acquired of the sun using the same apparatus as the camera sensitivity/filter transmissivity procedure to determine if the filters

maintained the same characteristics, given that the sun emits more UV light than the incandescent source used in the lab.

3.5 Hand Samples

Samples were cut using a rock saw, and then polished using 240 grit, silicon carbide polish to remove saw blade marks. Samples were washed to remove excess grit and left to air dry for 24 hours. Dried samples were placed perpendicular to the camera sensor, and the light source used in the camera calibration was directed at an angle of 25° to the sample surface.

Filters were wiped clean before every session and stored in a paper film in between images to reduce dust buildup. A section of PVC pipe was cut, inserted over the macro lens and attached to the bellows. The filter adapter was attached to the end of the pipe and a piece of cardboard was placed immediately beside the filter adaptor, in between the light source and the lens to reduce the possibility of light reflecting off of the filter in the space (~1 mm) between the filter and the end of the pipe.

3.6 File Conversion and Shutter Corrections

The RAW images were converted to TIFF files in order to separate each image into 3 images, one for each color band. A cartographic model (**Error!**

eference source not found.3-7) was then built in ArcMap to convert the TIFF files image by images, band by band to FLOAT files, which could then be imported as Idrisi raster files for image processing.

After file conversion, corrections were applied to account for varying exposure times from filter to filter using the TerrSet Macro Modeler. Pixel values were normalized by correcting different images of shutter speeds (exposure time) to the same shutter speed (1/60s), and the NIR removal process was executed using each filter's respective constant.

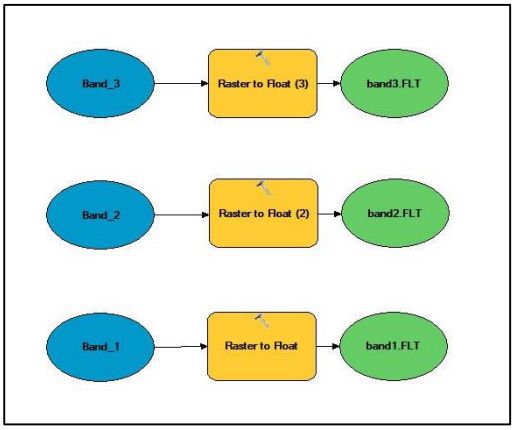

Figure 3-6. Sample of the ArcGIS cartographic model used in file conversion for the three bands of a single image.

Average pixel values were generated for each filtered image taken and plotted on a graph. Hand sample and outcrop averages were calculated by creating a mask image that eliminated sections of images that included anything besides granite (meter stick, tripod shadow, backdrop, etc.).

3.7 Lichen Removal

An NDVI calculation was used to identify and separate pixel values attributed to lichen on outcrops. A mask image was created by reclassifying lichen pixels that fell above an outcrop specific threshold of NDVI to a value of zero, and all others to a

value of one. Reclassification thresholds were tweaked for each sample image by visually comparing to the full outcrop image, to remove lichen pixels while maintaining as much unobstructed outcrop as possible. The Herring Cove outcrop contained very little lichen coverage, however the outcrop contained numerous depressions and pockmarks from erosion. The NDVI calculation was also effective at removing shadow marks from the depressions, as well as the lichen. The mask images for each outcrop site were then applied to generate outcrop specific average pixel values. Initial averages yielded large standard deviations due to the masking process. The data was constrained to values that formed a normal distribution, or as close to a normal distribution as the data allowed (figure 3-8).

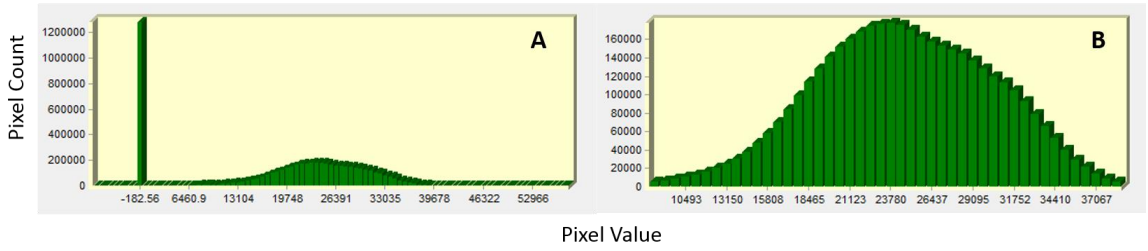

Figure 3-6. Pixel value distribution after lichen removal process. A) Distribution before constraints and B) after constraints.

During the calculation of average pixel values for the Herring Cove outcrop, images were separated into two different polygons to account for a slight change in the angle between the outcrop surface and the sun. This location was broken into two groups, HC upper and HC lower, to determine the significance of the slope change on pixel averages.

4.0 RESULTS and DISCUSSIONS

4.1 General Statement

The results of the spectral sensitivity measurements indicate why this study is purely comparative in nature. As with the other filtered images, the NIR images render 3 bands of data corresponding to radiance on the red, green, and blue sites of the CCD. Without a detailed knowledge of the specifications of the D40 sensor (Nikon does not release this information), it is impossible to determine if the total reflected NIR light is a sum of the 3 bands, or if there is redundancy across the 3 bands. A comparison between the three bands from multiple images indicates that the response is not variable. It is assumed in this study that the blue and green bands represent redundant reflected NIR information, and only the red band is considered.

Hand samples are briefly described and spectra acquired from 20 bellows images are compared to field image spectra. Where spectral characteristics of bellows images vary from the average trend among the samples, images are visually analyzed to determine the source of discrepancies. Aspects of data collection and processing reveal bias in the results and methods to reconcile bias are discussed. Finally, problems discovered in field measurements that contribute to error in the spectra are identified and discussed.

4.2 Sample Descriptions

Spryfield 1 (SP1):

The outer faces of the SP1 sample have distinct orange and red weathering products that are visible on the cut/polished face of the sample. Lichen coverage ranges from ~15% to 25%. The cut sections are relatively small due to difficulty in obtaining a large sample from the imaging location and each face has ~25 – 30 cm^2 of surface area suitable for imaging. The sample contains ~7 - 10% biotite, ~25% quartz, and equal parts remaining of feldspar and plagioclase.

Spryfield 2 (SP2):

A large (20 x 20 x 15 cm) sample was collected from the imaging area at outcrop SP2. Much like SP1, there is a ~15 to 25% range of lichen coverage on the outer faces with orange, and red/amber alteration products. The interior of this sample shows weathering products intruding ~0.5 – 1 cm from the outer face. The cut face is not mineralogically distinct from SP1, although the hand sample is sporadically megacrystic with the largest crystal measuring 4 x 2.5 cm.

Herring Cove (HC1 and HC2):

These two samples come from the same outcrop location, but are offcuts from different regions of the hand sample retrieved from the imaging site. They are almost mineralogically identical to SP1 & 2, but with a slightly lower quartz content. The cut faces also have the same surface area as SP1 and the outer faces contain very sparse (>5%) lichen coverage. The cut faces shows a different pattern of alteration; it is more pinkish/red and tends to surround phenocrysts in an almost dendritic fashion. It is probable that this is caused by the near shore location of the samples and subsequent wave action as opposed to SP1&2 which are located further inland.

4.3 Bellows Pixel Graphs

Pixel graphs of the shutter corrected bellows images show a spectrographic change between the Spryfield samples (SP1 and SP2) and the Herring Cove samples (HC1 and HC2). Graphs of the same samples taken at the same shutter speed showed no variation between the three locations. All bellows images have a consistent trend in the blue-green-red spectrum (figure 4-1). The most variation generally occurs in the 87 filtered images where the standard deviations are also comparably higher to the other filtered images, due to the bimodal distribution of

pixel intensities. Biotite, quartz, and feldspar form distinctive groups in the NIR, which causes the change in pixel distribution (figure 4-2). In the 400-480 nm region, HC samples have a slightly higher average value (5470) compared to SP1 samples (4548) and SP2 samples (3823). In the 480-590 nm region, HC1, HC2, and SP1 have comparable values (-783.6, -783.8, and -920.2 respectively).

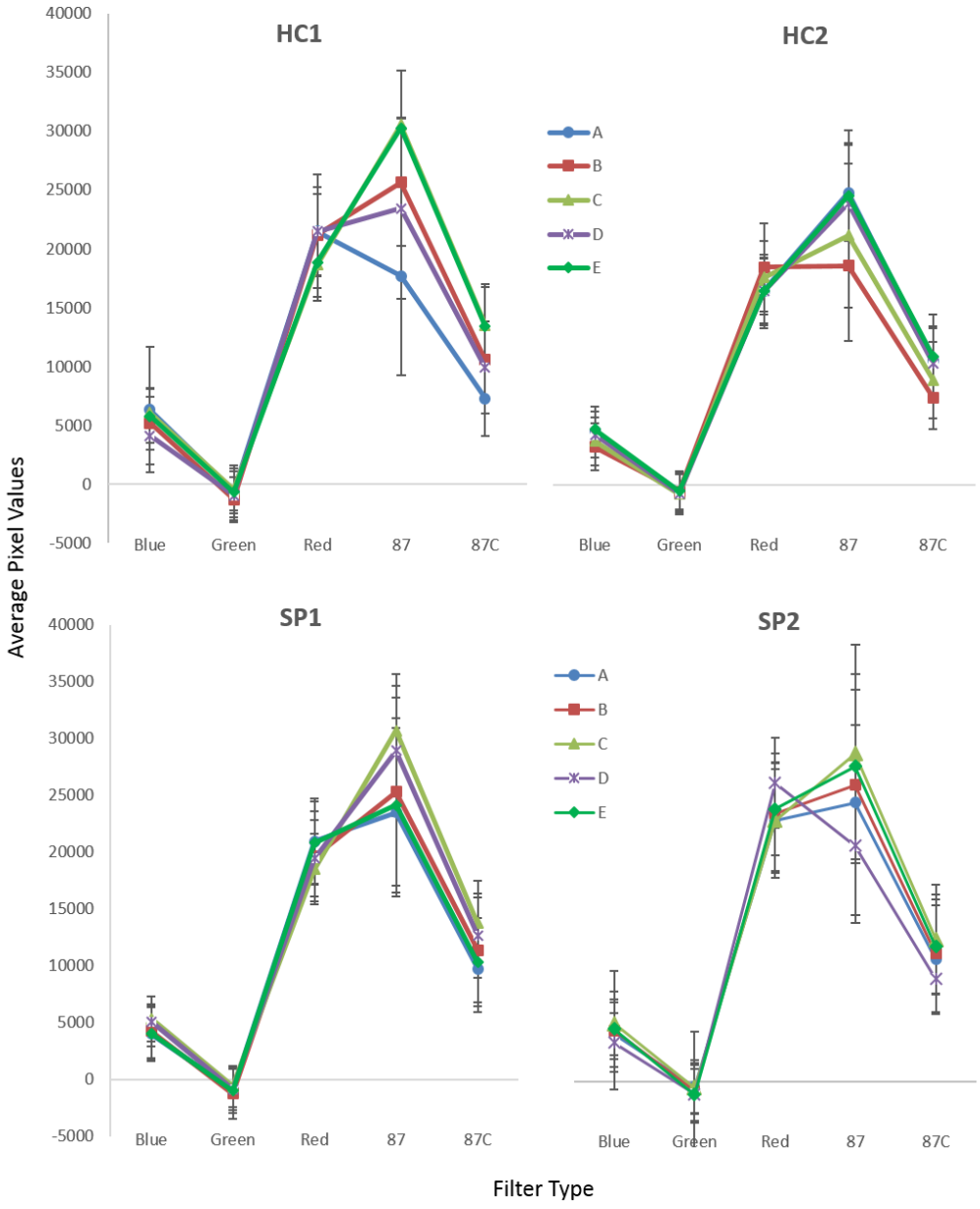

Figure 4-1. Average pixel graphs for bellows images. A-E refers to locations on the cut face of each hand sample.

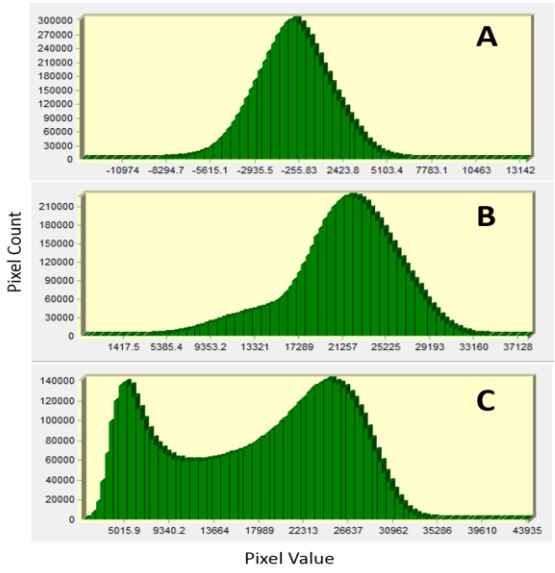

Figure 4-2. Pixel distribution change from green to red to NIR (A-C respectively) in sample HC1-A.

Samples SP2-D and HC1-A have identical red-87-87C signatures that are visibly different from the rest of the samples (figure 4-1). Instead of the characteristic spike in the 87 filtered region, these have a dip in the signature (see section 4.5).

4.4 Adjusted NIR Correction Procedure

Variation between the shutter corrected pixel graphs and graphs derived from images taken at the same shutter speed indicate that the exposure correction process skews the results. Holst (1998) states that the exposure time of a CCD is proportional to output. The original correction process involved normalizing two images of different exposure times to the same exposure time, and verifying that the average pixel value of the corrected image was the same for both images (figure 3-5). The process only accounted for average value changes to the image as a whole, and not the specific NIR region in the image. To determine the accuracy of the shutter corrections specifically in the NIR region, the light source spectral images

from the calibration process were re-analyzed. A polygon was digitized in the NIR region of two 87 filtered images, taken at shutter speeds of 0.77s and 0.5s. The latter image was multiplied by 1.54 to correct to the 0.77 exposure time and statistics for the 0.77s image and the corrected 0.5s image were generated (table 4-1).

Table 4-1. Original shutter correction process with direct focus on the NIR region of filtered images.

Filter	Shutter Speed (s)	Correction Factor	Original NIR Average	Final Average
87	0.77	-	125.5	125.5
Blue	1.6	0.48125	183.8	88.4
87	0.77	-	191.6	191.6
87	0.5	1.54	171.9	264.6
87C	0.77	-	129.4	129.4
87C	1.6	0.48125	176.5	85

The original process generates new values either too high or too low in the NIR region. An alternate method is to determine a constant based on the change in NIR region averages between two images of different exposure times. The long exposure image is divided by the short exposure image, producing a value to correct the short to the long exposure image:

$$I_{corr} = I_2 \times \left[\frac{I_{1avg}}{I_{2avg}}\right]$$

Where I_{1avg} *= Long exposure image average pixel value*

I_{2avg} *= Short exposure image average pixel value*

I_2 *= Short exposure full image*

Similarly, the long exposure image can be corrected to the average value of the short exposure image:

$$I_{corr} = \frac{I_1}{\left[\left[\frac{I_{1avg}}{I_{2avg}}\right]\right]}$$

This process more accurately corrects for shutter differences than the previous method (table 4-2). An overlay with the 87 image subtracted from the newly corrected blue image generates an average pixel value of -0.26 in the NIR region of the overlay image, indicating that the lab and field blue filtered images are under-corrected in the NIR.

Table 4-2. Original shutter correction process with focus on only the NIR region.

Filter	Shutter Speed (s)	Correction Factor	Original NIR Average	Final Average
87	0.77	-	125.5	125.5
Blue	1.6	1.4645	183.8	125.49
87	0.77	-	191.6	191.6
87	0.5	1.1146	171.9	191.5
87C	0.77	-	129.4	129.4
87C	1.6	1.364	176.5	129.4

Compared to spectrographic values of granites from Kerr et al. (2011), it is probable that under-correction is the cause of the negatively sloped blue-green trend in the bellows images (figure 4-3B). Constants for the green and red NIR correction were determined from spectra taken at the same exposure time, and do not require further correction.

4.5 Multispectral Bellows Images

Pixel intensity scales for each image are sample specific and each image measures 0.85 cm across. The bounds are set by the lowest and highest pixel value in the set, corresponding to the blue and 87 images, respectively. Biotite is most distinguishable in the NIR bands, lowering the NIR average pixel values as it increases in abundance. It is probable that this is due to the ~900 nm absorption feature and to a lesser extent, the 714 nm absorption feature reported by Smith (1978) in reference to Faye (1968) and Robbins and Strens (1972). Quartz also has some influence in the 87 pixel average shift as it has lower NIR values than the feldspars, but higher than biotite (figure 4-4). The shift does occur within the error bars, however the errors are standard deviation, which assumes a normal distribution (e.g. see figure 4-2C).

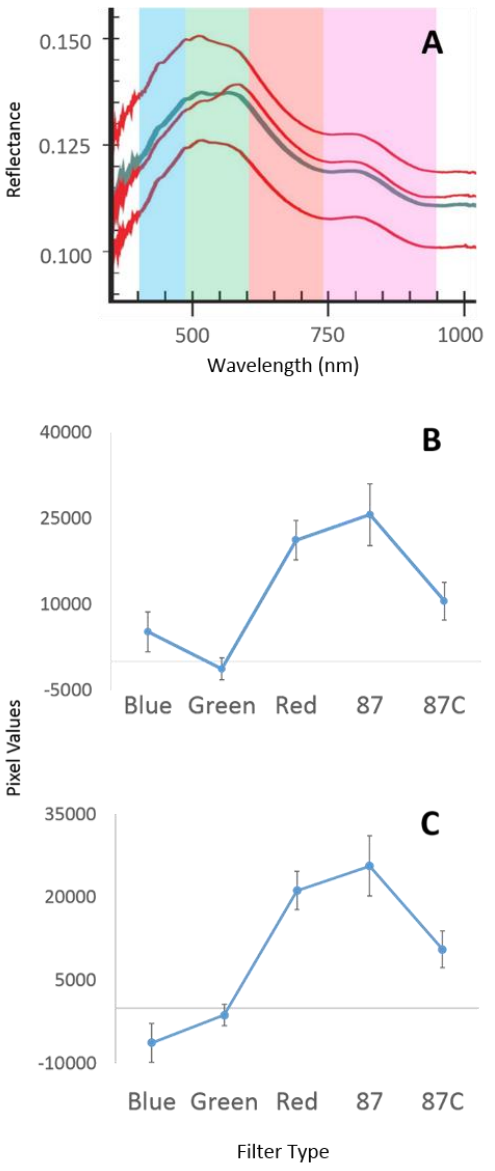

Figure 4-3. Comparative whole rock spectra. A) Granite spectra from the Moly Brook deposit, Southern Newfoundland. Red lines are single samples, grey line is an average of the three. Kerr et al. (2011). Blue, green, red, and NIR (pink) bands are superimposed for comparison with filter averages in B and C. B) Average pixel graph of HC1-B with original NIR correction procedure. C) Average pixel graph of HC1-B with adjusted correction prodecure.

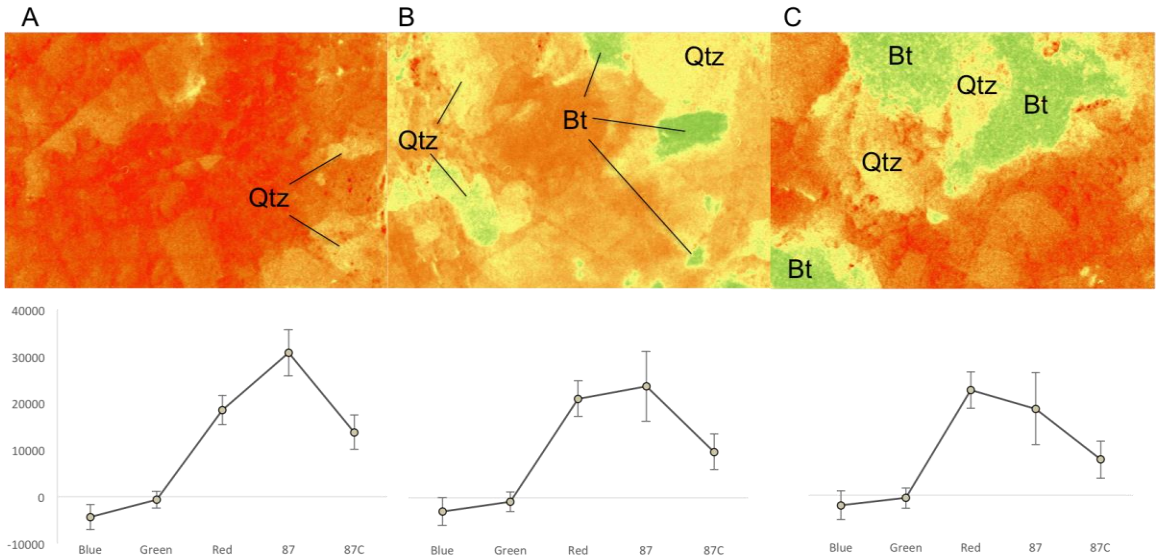

Figure 4-4. Effect of increased biotite content on average pixel graphs in the 87 region. All images are taken with the 87 filter. A) SP1-C, B) SP1-A, C) HC1-A.

In comparison, the 87C-filtered values show little change from sample to sample, despite peak transmission near the 900 nm absorption band (figure 3-4). The CCD sensitivity drops more drastically as the wavelength increases in the IR region and changes due to biotite and quartz composition are far more subtle. Identifying compositional variation from pixel graphs is problematic. Quartz and biotite both cause the pixel graphs to change in the NIR region, but it is not evident

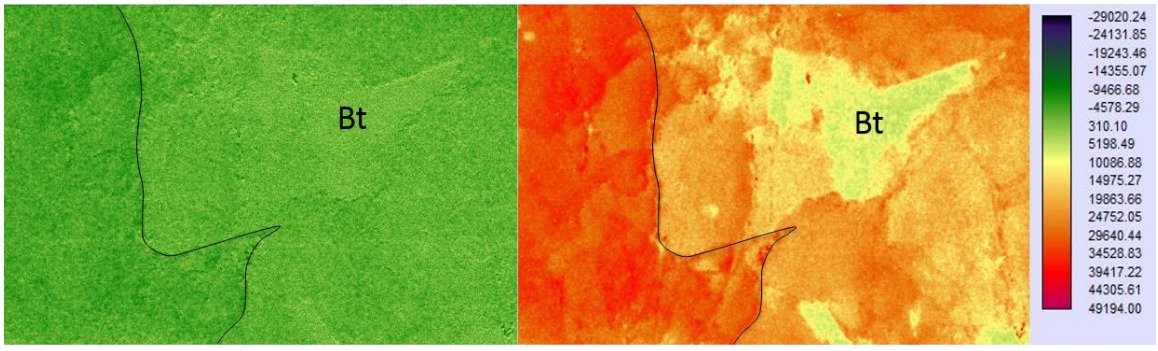

Figure 4-5. Effect of spectral bias in the NIR correction procedure on a corrected blue image (HC1-D).

from the graphs what the ratio of the two minerals is based on this change, and larger biotite crystals have an influence on the spectral response of quartz when they occur together.

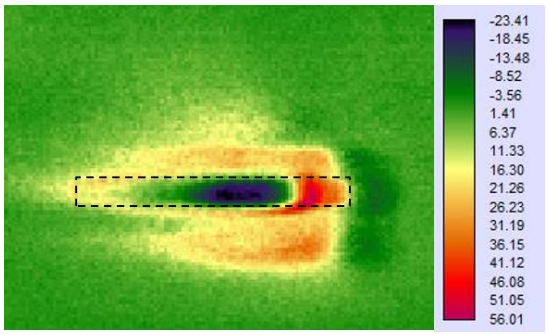

Figure 4-7. NIR light spectrum from sensitivity measurements displays spectral bias after the correction procedure.

Features are visible in the blue and green filtered images. It is probable that this is the result of the NIR correction process, and not absorption features in those spectral regions (figure 4-5). In addition to compounding noise from the overlay function, the adjusted NIR correction process removes only NIR light representative of an average across the region. The process retains some wavelength bias, undercompensating in the ~775-800 nm region and overcompensating in the ~830-860 nm region (figure 4-6).

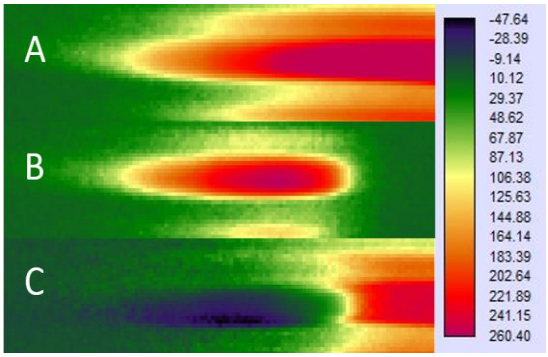

Figure 4-6. Correction process on red filtered spectrum A) Uncorrected light spectrum with red filter. B) Uncorrected light spectrum with 87 filter. C) Corrected spectrum after NIR removal procedure.

NIR corrections for red filtered images retain less wavelength bias, and are the closest to true reflected values out of the blue, green, and red filtered images (figure 4-7). Comparison between the red and NIR images indicate that the NIR images show crystallographic orientation and surface depressions more clearly (figure 4-8). Surface depressions appear as discrete spots in the NIR images, or around grain boundaries (figure 4-8, B and F).

The pixel intensity of minerals is also largely dependent on their orientation in the NIR region. Biotite in the red filtered images has a more speckled appearance,

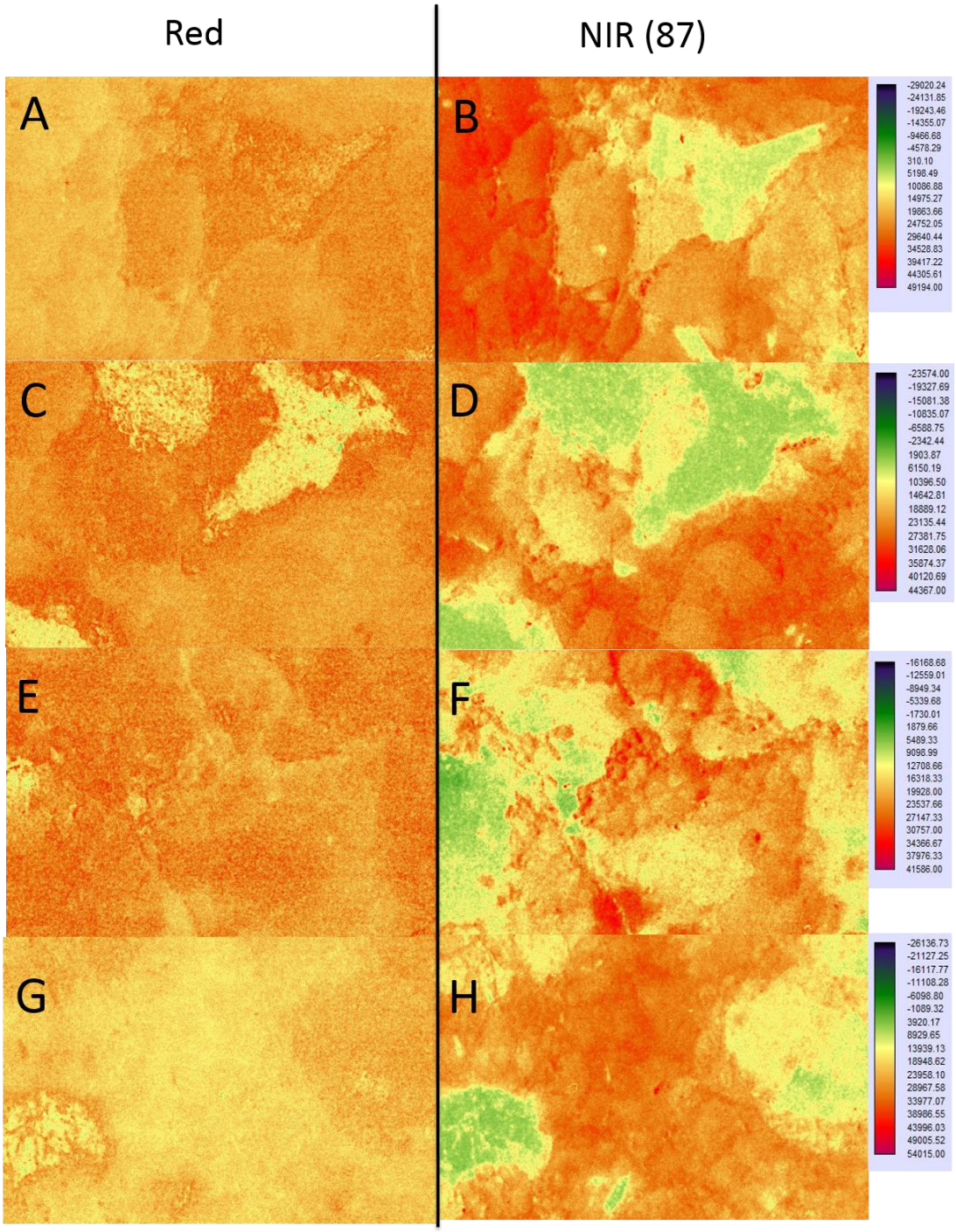

Figure 4-8. . Samples HC1-D, HC1-A, SP2-D, and SP1-E from top to bottom. Scales are normalized to the lowest (blue image for each sample) and highest pixel values of each sample set.

indicating that reflected light in the red wavelengths display surface roughness more than crystallographic orientation (figure 4-8 C/D and G/H). Broad mineral boundaries are still visible, and minerals are more easily distinguished depending on their comparative orientations. Multispectral images of feldspars indicate that they can only be distinguished from biotite and quartz by comparison in the red to NIR wavelengths but distinction between feldspar species is not reliable with the data available in this study. Variation in feldspar pixel value intensities may be related to their relative FeO content as reported by Adams and Goullaud (1978) (see figure 2-5). The high value region in figure 4-8B may be indicative of this instead of crystallographic orientation, however further work is needed for verification.

4.6 Field Image Pixel Graphs

Field images produced variable results. Only data from SP2 displays the same blue to green spectral trend as the fine scale images. All field locations show a decreasing trend from the red to NIR range, compared to the increasing trend from

Table 4-3. Average pixel values of two sections of the Herring Cove outcrop.

	HC Lower		HC Upper	
Filter	Avg	Std	Avg	Std
Blue	33408	4000	33275	4423
Green	35656	3195	35761	3556
Red	52616	1143	52507	1298
87	9783	506	9575	687
87C	13802	951	13369	1158

the fine scale data. Besides this single trend, the remainder of the SP2 trend is not

comparable to the bellows images. In the NIR range, only the SP1 graph maintains the negative pixel value trend from the 87 images to the 87C images shown from the bellows images. All other locations show an increase in pixel values in the two regions.

HC lower and HC upper have an identical signature. The average pixel values between the two sections range by a measure of a few hundred pixel values, with HC lower having higher values than HC upper, the exception being the green band. It is probable that the angle change at this scale is insignificant given that there is little variation between the two sections (table 4-3). All locations display the highest

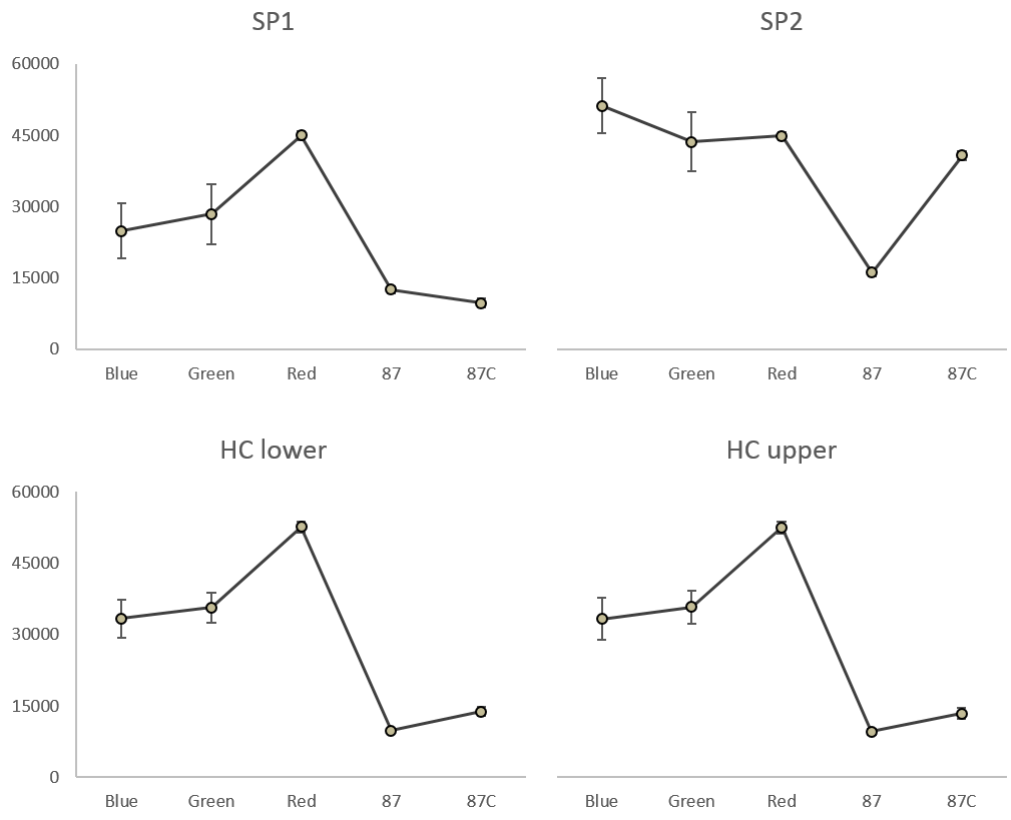

Figure 4-9. Average field pixel graphs of outcrop sites.

standard deviations in the blue and green filtered regions, mainly due to overexposure of images in the red and NIR images.

Comparison of field pixel graphs indicates that they are more a representation of shutter speed variations than outcrop variation (table 4-4). Images acquired in the blue-green-red spectra of SP1 and HC were taken at the same shutter speed and have an identical trend compared to SP2 which was taken at a different shutter speed, further spectral variations are consistent with shutter speed variations from site to site.

Table 4-1. Shutter speeds (exposure time) for filtered images at each outcrop site.

Site number	Filter	Shutter Speed
SP1	Tri-blue	1/2500s
	Tri-green	1/2500s
	Tri-red	1/2500s
	87C	1/500s
	87	1/500s
SP2	Tri-blue	1/320s
	Tri-green	1/800s
	Tri-red	1/800s
	87C	1/800s
	87	1/200s
HC	Tri-blue	1/2500s
	Tri-green	1/2500s
	Tri-red	1/2500s
	87C	1/640s
	87	1/400s

The most significant change from the field graphs and the bellows graphs is in the NIR range. Bellows graphs have high values in the NIR and field images have low values. There are several possibilities for this change. The incandescent source used for the bellows images has different spectral characteristics than the sun, and is more spectrally biased in the red and NIR regions. Field images were taken at different exposures and were corrected based on exposure time. In section 4.4, it was determined that detected NIR light is not linearly related to exposure time, and correcting a long exposure image to a short exposure image overshoots the true

value (table 4-1). Without a set of filtered images taken at the same exposure time, it is impossible to determine what effect the light source change has on average pixel graphs, or how the spectra would be altered by images taken at the same shutter speeds. It is probable that grain size also contributes to pixel graph changes. The outcrops are megacrystic, however none of the samples that were obtained for lab analysis contained megacrysts, and comparative analysis of variation due to megacrysts on bellows pixel graphs could not be completed.

4.7 Multispectral Field Images

While in the field, red filtered images appeared to be appropriately exposed compared to the other filtered images. The mechanics of the camera proved to be misleading, for when the red filtered images were isolated into their respective color bands, the green and blue bands provided clear images, yet the red bands were drastically overexposed. The overexposure and subsequent blooming creates a very small standard deviation in the data.

The sensor theory related to overexposure implies that an overexposed pixel is the result of a photosite that has been overfilled with photons. It follows that this should correspond to the pixel value with the greatest intensity. The pixel histograms for NIR corrected and overexposed images do not show this pattern, but instead show three pixel population groups.:(1) a low intensity group that approaches the peak of a normal distribution, (2) a highly populated group of

similar intensity values, and (3) a group of intensity values higher than (1), lower than (2), and declining in population from the peak of a normal distribution (figure 4-11). This habit results from the NIR correction process.

Despite using a tripod for the field images to keep the camera stationary, there are slight changes in the (x,y) locations of a pixel from image to image as a result of pressing the button to take the picture, changing the exposure time, and possibly exchanging filters. The changes are indistinguishable from the image as a whole, but can be identified when a small region of the image is enlarged (figure 4-12).

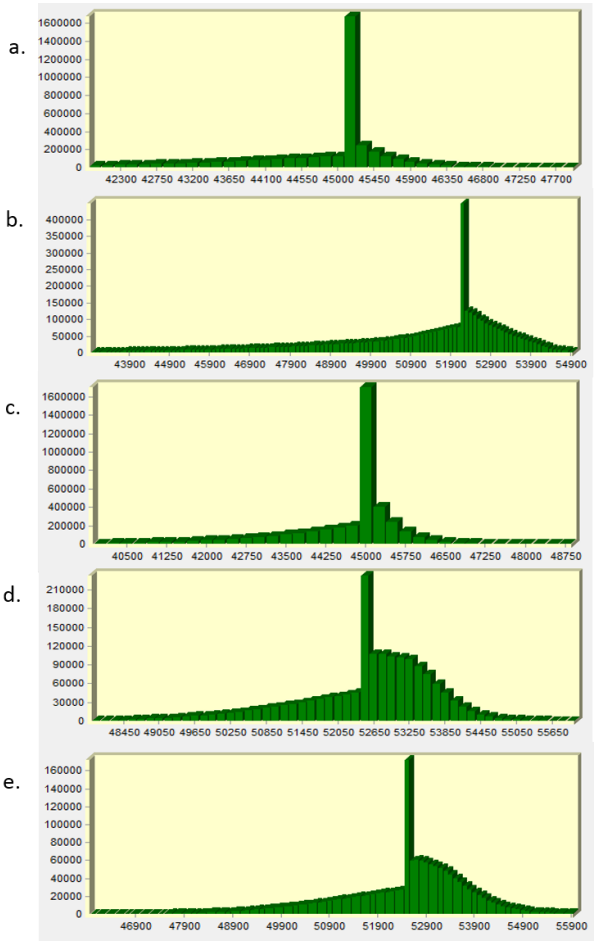

Figure 4-10. Histograms of overexposed and NIR corrected field images with pixel intensity value on the x-axis and pixel count on the y-axis. Graphs a-e correspond to SP1-red, SP2-blue, SP2-red, HC lower-red, and HC upper-red, respectively.

The 87 filtered images used to remove NIR from the uncorrected red, green, and blue filtered images are also overexposed to varying degrees. It is probable that the overexposed values in each image correspond to the same real location on the outcrop. To verify, pixel values in the uncorrected red HC outcrop image (with lichen removed) were reclassified to a value of 1 for overexposed pixels, determined by narrowing the histogram display and class

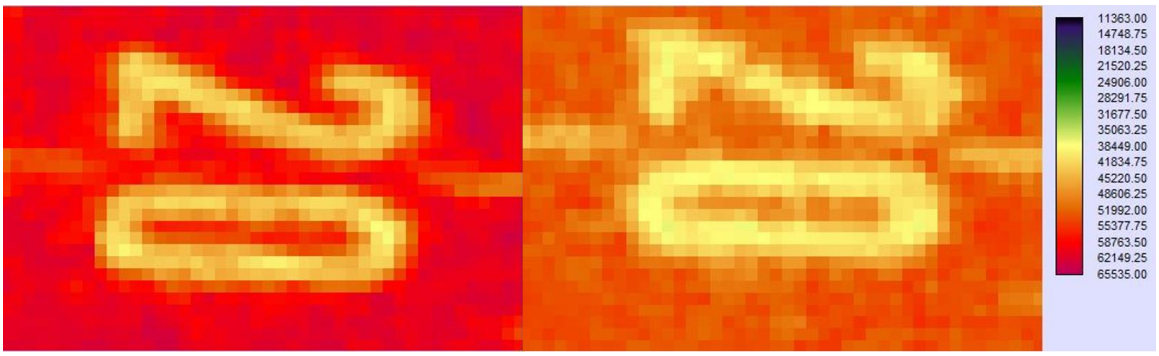

Figure 4-12. Two enlarged images of the meter stick taken with the red filter (left) and 87 filter (right) showing slight camera shift.

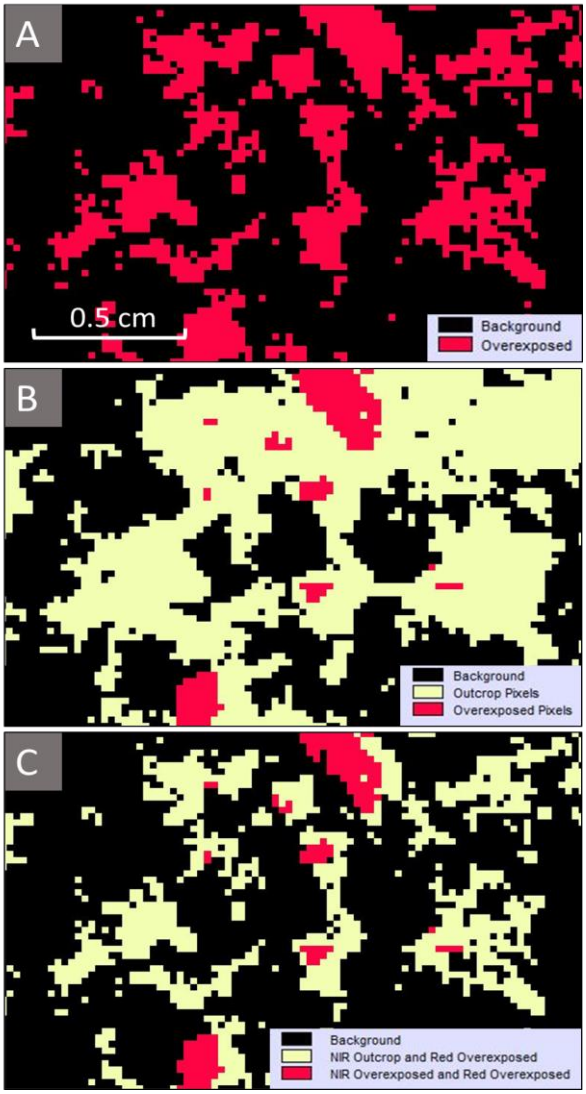

Figure 4-11. Consistency of overexposed pixel overlap. A) Overexposed pixels in red filtered HC outcrop image. B) Outcrop and overexposed pixels in 87 filtered HC outcrop image. C) Multiplied overlay image.

width. By inspection, the overexposed values fell between an intensity of 65525 and 65535. All other values were reclassified as 0's (figure 4-12A). The scaled NIR correction image was reclassed into three groups: 1) Overexposed pixels (values between 10475 and the max value of 10485.12) with a new value of two, 2) outcrop pixels that fell within the lichen free reclassification (6400 to <10475) with a new value of one, and 3) background pixels omitted by the lichen removal reclassification, with a new value of zero (figure 4-12B). The first image was multiplied by the second image to spatially determine how often the

overexposed pixels overlap (figure 4-12C).

The result indicates why the NIR removal process for overexposed images separates the final histogram into three populations (figure 4-13). If the two images are perfectly aligned, the peak from figure 4-13A would translate to the ~55000 region of figure 4-13C.

Since the pixel locations are not identical, there is a variable range of intensities that subtract from the overexposed sites. It is probable that the pixels belonging to the peak population in figure 4-12A are subtracting from surrounding pixels belonging to the peak population in figure 4-12B.

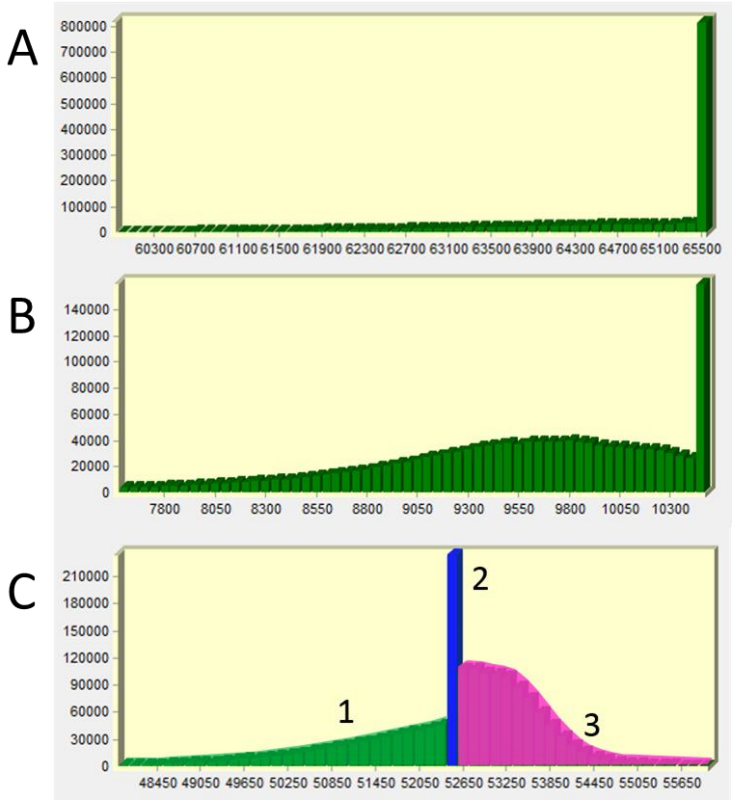

Figure 4-13- Pixel distributions of the HC outcrop image. A) Red filtered image, B) 87 filtered image, C) corrected red image.

5.0 CONCLUSION

The results of this study reveal some clear points for imaging spectroscopy.

Consumer CCDs are problematic for scientific analysis. The filter configuration of the sensor is often protected by the manufacturer and is produced for the purpose of optimizing aesthetics, not raw data or collecting NIR light.

Light filters must be able to block out all incoming light except for the chosen wavelengths for the analysis. Although the correction procedure removed nearly all of the NIR light, the process is only able to remove an average across the NIR region detected by the sensor, and bias remains in some narrow regions of the NIR spectrum.

The spectral resolution of the filters are too wide for detection and spatial analysis of specific absorption features. In the case of REEs, absorption features can be as narrow as 10 nm (Kerr et al., 2011). It follows that by narrowing the spectral resolution of a fine scale CCD imaging system, absorptive features can be more clearly recognized, and REE distributions may be visually displayed without the need of a scanning electron microscope or x-ray fluorescence analysis.

There is definite potential for future work in imaging spectroscopy. As Kerr et al. (2011) reports, there is a great need for a standardized, peer reviewed collection procedure for visible to NIR spectroscopic data. Much of the spectral data from the USGS spectral library is generated from crushed samples, which can complicate whole image analysis. Many of the samples in this study represented

variable signatures due to a combination of mineral occurrences, such as the influence of biotite on pixel value intensity of quartz. The issue of an absorbance spectrum containing responses from multiple different minerals in natural samples is also reported by Kerr et al. (2011).

The methods in this study largely revolved around corrections that introduce error. Absorption features can be shallow, and slight errors can overprint these features. An ideal setup would involve the following:

1) An unfiltered, cooled sensor to reduce dark current and shot noise (multiple sensors could also be used to quantify the significance of manufacturer variation from sensor to sensor)
2) A monochromator to separate light into narrow wavelength bands, removing the need for filters
3) A spectrally flat light source, or a detailed spectra of the light source for wavelength bias corrections
4) A system to enable image collection in the field that would eliminate the need to touch the camera in between images.

There also remains the possibility of advancing this study to the scale of satellite platforms, which presently have advanced to a sub centimeter spatial resolution. Once errors outlined in this study are removed, it may be possible to maintain a spectral signature from the bellows scale to the outcrop scale, and ultimately to satellite platforms. Investigating the possibility of generating accurate

whole rock spectra from satellites would have profound implications for geological analysis on Earth, as well as other planets, however a great deal of future study in this field is required.

6.0 REFERENCES

Adams, J.B. (1975), Interpretation of visible and near infrared diffuse reflectance spectra of pyroxenes and other rock-forming minerals, *Infrared and Raman Spectroscopy of Lunar and Terrestrial Minerals*, edited by C. Karr Jr., Academic Press, New York, pp.91-116.

Adams, J.B., and Lee H. Goullaud (1978), Plagioclase feldspars: Visible and near infrared diffuse reflectance spectra as applied to remote sensing*, Proc. Lunar Sci. Conf. 9th*, pp. 2901-2909.

Cormier, R.F. and T.E. Smith (1973), Radiometric Ages of Granitic Rocks, Southwestern Nova Scotia, *Canadian Journal of Earth Sciences,* 10, pp. 1201-1210.

Clark, R.N. and A.N. Rencz (Eds.) (1999), *Remote Sensing for the Earth Sciences: Manual of Remote Sensing,* 3rd ed., pp.728, John Wiley & Sons Inc., New York, NY.

Clark, R.N., G.A. Swayze, A.J. Gallagher, T.V.V. King, and W.M. Calvin (1993), The U.S. Geological Survey, Digital Spectral Library: Version 1:0.2 to 3.0 µm, *Open File Report 93-592*, pp.1326, U.S. Geological Survey, Denver, CO.

Clarke, D.B., G.K.C. Clarke (1998), Layered granodiorites at Chebucto Head, South Mountain batholith, Nova Scotia, *Journal of Structural Geology,* 20-9/10, pp. 1305-1324.

Feng, J., B. Rivard, A. Gallie, and A. Sanchez-Azofeifa (2011), Rock type classification of drill core using continuous wavelet analysis applied to thermal infrared reflectance spectra, *International Journal of Remote Sensing,* 32-16, pp. 4489-4510.

Fujiwara, Akira and Yasuo Takahashi (2001), Manipulation of elementary charge in a silicon charge-coupled device, *Nature*, 410-6828, pp. 560-562.

Galbán, J., S. de Marcos, I. Sanz, C. Ubide, and J. Zuriarrain (2010), CCD detectors for molecular absorption spectrophotometry. A theoretical and experimental study on characteristics and performance, *Analyst,* 135, pp. 564-569.

Gates, D.M. (1980), *Biophysical Ecology,* Springer-Verlag, New York, NY.

Hamilton, V.E. (2010), Thermal infrared (vibrational) spectroscopy of Mg–Fe olivines: A review and applications to determining the composition of planetary surfaces, *Chemie der Erde*, 70, pp. 7-33.

Hecker, C., J.H. Dilles, M. van der Meijde, and F.D. van der Meer (2012), Thermal infrared spectroscopy and partial least squares regression to determine mineral modes of granitoid rocks, *Geochemistry Geophysics Geosystems,* 13-3, pp. n/a.

Jenson, J.R. and K.C. Clarke (Eds.) (2005), *Introductory Digital Image Processing, A Remote Sensing Perspective,* 3rd ed., 526 pp., Pearson Education Ltd., Upper Saddle River, NJ.

Kerr, A., H. Rafuse, G. Sparkes., J. Hinchey, and H. Sandeman (2011), Visible/infrared spectroscopy (VIRS) as a research tool in economic geology: background and pilot studies from Newfoundland and Labrador, *Current Research, Report 11-1,* pp. 145-166, Newfoundland and Labrador Department of Natural Resources, Geologic Survey, Mineral Deposits Section.

Longhi, J., D. Walker, and J.F. Hayes (1976), Fe and Mg in plagioclase*, Proc. Lunar Sci. Conf. 7th*, pp. 1281-1300

Life Pixel (2015), Chapter 2 - Basic Theory - How Filters Work, http://www.lifepixel.com/infrared-photography-primer/ch-basic-theory-how-filters-work

Litwiller, D. (2005), CMOS vs. CCD: Maturing Technologies, Maturing Markets, *Photonics Spectra*, 39-8.

Lyon, R.J.P., and E.B. Burns (1963), Analysis of Rocks and Minerals by Reflected Infrared Radiation, *Economic Geology,* 58, pp. 274-284.

Macdonald, M.A. (2001), Geology of the South Mountain Batholith, Southwestern Nova Scotia, *Open File Report ME 2001-2*, pp. 372, Department of Natural Resources, Minerals and Energy Branch, Halifax, Nova Scotia.

MacDonald, M.A. and R.J. Horne (1988), Petrology of the zoned, peraluminous Halifax Pluton, south-central Nova Scotia, *Atlantic Geology*, 24, pp. 33-45.

McKenzie, C.B., and D.B. Clarke (1975), Petrology of the South Mountain Batholith, Nova Scotia, *Canadian Journal of Earth Sciences,* 12, pp. 1209-1218.

Miller, P. (1979), The evolution of tin bearing fluids in the Devonian granitoid rocks of the Halifax Pluton, Nova Scotia, M.Sc. dissertation, pp. 131, University of Windsor, Windsor, Ontario, Canada.

Naganuma, T., Y. Kagawa (1999), Effect of particle size on light transmittance glass particle dispersed epoxy matrix optical composites, *Acta Materiala,* 47-11, pp. 4321-4327.

Nemani, R.R., and S.W. Running (1989), Estimation of Regional Surface Resistance to Evapotranspiration from NDVI and Thermal-IR AVHRR Data, *Journal of Applied Meteorology,* 28, pp.276-284.

Ninomiya, Y., B. Fu, and T.J. Cudahy (2005), Detecting lithology with Advanced Spaceborne Thermal Emission and Reflection Radiometer (ASTER) multispectral thermal infrared "radiance-at-sensor" data, *Remote Sensing of Environment,* 99, pp. 127-139.

Olthof, I., D. Pouliot, R. Latifovic, and W. Chen (2008), Recent (1986-2006) Vegetation-Specific NDVI Trends in Northern Canada from Satellite Data, *Arctic*, 61-4, pp.381-394.

Smith, T.E. (1974), The Geochemistry of the Granitic Rocks of Halifax County, Nova Scotia, *Canadian Journal of Earth Sciences,* 11, pp. 650-657.

Smith, T.E. and A. Turek (1976), Tin-Bearing Potential of some Devonian Granitic Rocks in S.W. Nova Scotia, *Mineralium Deposita*, 11, pp. 234-245.

7.0 APPENDICES

Uploaded as separate files.